研究成果の刊行に関する一覧表

雑誌

発表者氏名	論文タイトル名	発表誌名	巻号	ページ	出版年
Liu HJ, Moroi S, Yasumoto S, Koga T, Masuda T, Chen QJ, Tu YT, Fure M, Aburatani H, Urabe K.	Expression of elafin in extramammary Paget's disease.	Br J Dermatol.	152(3)	578-9	2005
Hanada T, Tanaka K, Matsumura Y, Yamauchi M, Nishinakamura H, Aburatani H, Mashima R, Kubo M, Kobayashi T, Yoshimura A.	Induction of hyper Th1 cell-type immune responses by dendritic cells lacking the suppressor of cytokine signaling-1 gene.	J Immunol.	174(7)	4325-32	2005
Komura D, Nakamura H, Tsutsumi S, Aburatani H, Ihara S.	Multidimensional support vector machines for visualization of gene expression data.	Bioinformatics	21(4)	439-44	2005
Inozume T, Matsuzaki Y, Kurihara S, Fujita T, Yamamoto A, Aburatani H, Shimada S, Kawakami Y.	Novel melanoma antigen, FCRL/FREB, identified by cDNA profile comparison using DNA chip are immunogenic in multiple melanoma patients.	Int J Cancer.	114(2)	283-90	2005
Harada, M., Qin, Y., Takano, H., Minamino, T., Zou, Y., Toko, H., Ohtsuka, M., Matsuura,K., Sano, M., Nishi, J., Akazawa, H., Kunieda, T., Zhu, W., Hasegawa, H., Kunisada, K., Nagai, T., Nakaya, H., Yamauchi-Takihara, K., Komuro, I.	G-CSF prevents cardiac Remodeling after myocardial infarction by activating Jak/Stat in cardiomyocytes.	Nat Med	11	305-311	2005
Nakahara T, Urabe K, Fukagawa S, Uchi H, Inaba K, Furue M, Moroi Y.	Engagement of human monocyte-derived dendritic cells into interleukin (IL)-12 producers by IL-1b + interferon (IFN)-g.	Clin Exp Immunol	139	476-82	2005

Morita K, Urabe K, Moroi Y, Koga T, Nagai R, Horiuchi S, Furue M.	Migration of keratinocytes is impaired on glycated collagen I.	Wound Repair Regen	13	93-101	2005
Saeki H, Iizuka H, Mori Y, Akasaka T, Takagi H, Kitajima Y, Tezuka T, Tanaka T, Hide M, Yamamoto S, Hirose Y, Kodama H, Urabe K, Furue M, Kasagi F, Torii H, Nakamura K, Morita E, Tsunemi Y, Tamaki K.	Prevalence of atopic dermatitis in Japanese elementary schoolchildren.	Br J Dermatol	152	110-4	2005
Yamaguchi T, Ohshima K, Karube K, Tutiya T, Kawano R, Suefuji H, Shimizu A, Nakayama J, Suzumiya J, Moroi Y, Urabe K, Furue M, Koga T, Kikuchi M.	Clinicopathological features of cutaneous lesions of adult T-cell leukaemia / lymphoma.	Br J Dermatol	152	76-81	2005
Kobayashi J, Inai T, Morita K, Moroi Y, Urabe K, Shibata Y, Furue M.	Reciprocal regulation of permeability through a cultured keratinocyte sheet by IFN-gamma and IL-4.	Cytokine	7	186-9	2005
Houjun Liu, Yoichi Moroi, Shinichiro Yasumoto, Hisashi Kokuba, Shinichi Imafuku, Tetsuya Koga, Teiichi Masuda, Yating Tu, Masutaka Furue, Kazunori Urabe.	Immunohistochemical localization of activated Stat3 and hTERT protein in psoriasis vulgaris.	Br J Dermatol			in press
Ge X, Yamamoto Shogo, Tsutsumi Shuichi, Midorikawa Yutaka, Ihara Sigeo, Wang SM, Aburatani H.	Interpreting expression profiles of cancers by genome-wide survey of breadth-of-expression in normal tissues..	Genomics			in press

Midorikawa Y, Tsutsumi S, Nishimura K, Kamimura N, Kano M, Sakamoto H, Makuuchi M, Aburatani H.	Distinct chromosomal bias of gene expression signatures in the progression of hepatocellular carcinoma.	Cancer Res.	64(20)	7263-70	2004
Minami T, Horiuchi K, Miura M, Abid R, Takabe W, Kohro T, Ge X, Aburatani H, Hamakubo T, Kodama T, Aird WC.	VEGF- and thrombin-induced termination factor, down syndrome critical region-1, attenuates endothelial cell proliferation, and angiogenesis.	J Biol Chem.	279(48)	50537-54	2004
Miyachi H, Ikebukuro K, Yano K, Aburatani H, Karube I.	Single nucleotide polymorphism typing on DNA array with hydrophobic surface fabricated by plasma-polymerization technique.	Biosens Bioelectron.	20(2)	184-9	2004
Kamei Y, Miura S, Suzuki M, Kai Y, Mizukami J, Taniguchi T, Mochida K, Hata T, Matsuda J, Aburatani H, Nishino I, Ezaki O.	Skeletal muscle FOXO1 (FKHR)-transgenic mice have less skeletal muscle mass, down-regulated type I (slow twitch / red muscle) fiber genes, and impaired glycemic control.	J Biol Chem.	279(39)	41114-23	2004
Watanabe T, Akishita M, Nakaoka T, He H, Miyahara Y, Yamashita N, Wada Y, Aburatani H, Yoshizumi M, Kozaki K, Ouchi Y.	Caveolin-1, Id3a and two LIM protein genes are upregulated by estrogen in vascular smooth muscle cells.	Life Sci.	75(10)	1219-29	2004
Takasato M, Osafune K, Matsumoto Y, Kataoka Y, Yoshida N, Meguro H, Aburatani H, Asashima M, Nishinakamura R.	Identification of kidney mesenchymal genes by a combination of microarray analysis and Sall1-GFP knockin mice.	Mech Dev.	121(6)	547-57	2004
Kohro T, Tanaka T, Murakami T, Wada Y, Aburatani H, Hamakubo T, Kodama T.	A Comparison of Differences in the Gene Expression Profiles of Phorbol 12-myristate 13-acetate Differentiated THP-1 Cells and Human Monocyte-derived Macrophage.	J Atheroscler Thromb.	11(2)	88-97	2004

Ogihara T, Asano T, Katagiri H, Sakoda H, Anai M, Shojima N, Ono H, Fujishiro M, Kushiyama A, Fukushima Y, Kikuchi M, Noguchi N, Aburatani H, Gotoh Y, Komuro I, Fujita T.	Oxidative stress induces insulin resistance by activating the nuclear factor-kappaB pathway and disrupting normal subcellular distribution of phosphatidylinositol 3-kinase.	Diabetologia.	47(5)	794-805	2004
Takita J, Ishii M, Tsutsumi S, Tanaka Y, Kato K, Toyoda Y, Hanada R, Yamamoto K, Hayashi Y, Aburatani H.	Gene expression profiling and identification of novel prognostic marker genes in neuroblastoma.	Genes Chromosomes Cancer.	40(2)	120-32	2004
Matsuo K, Galson DL, Zhao C, Peng L, Laplace C, Wang KZ, Bachler MA, Amano H, Aburatani H, Ishikawa H, Wagner EF.	NFAT rescues osteoclastogenesis in precursors lacking c-Fos.	J Biol Chem.	279(25)	26475-80	2004
Fujiwara K, Ochiai M, Ohta T, Ohki M, Aburatani H, Nagao M, Sugimura T, Nakagama H.	Global gene expression analysis of rat colon cancers induced by a food-borne carcinogen, 2-amino-1-methyl-6-phenylimidazo[4,5-b]pyridine.	Carcinogenesis.	25(8)	1495-505	2004
Hippo Y, Watanabe K, Watanabe A, Midorikawa Y, Yamamoto S, Ihara S, Tokita S, Iwanari H, Ito Y, Nakano K, Nezu J, Tsunoda H, Yoshino T, Ohizumi I, Tsuchiya M, Ohnishi S, Makuuchi M, Hamakubo T, Kodama T, Aburatani H.	Identification of Soluble Amino Terminal Fragment of Glypican-3 as a Serological Marker for Early Stage Hepatocellular Carcinoma.	Cancer Research	64(7)	2418-2423	2004
Nakatani N, Aburatani H, Nishimura K, Semba J, Yoshikawa T.	Comprehensive expression analysis of a rat depression model.	Pharmacogenomics J.	4(2)	114-26	2004

Mukasa A, Ueki K, Ge X, Ishikawa S, Ide T, Fujimaki T, Nishikawa R, Asai A, Kirino T, Aburatani H.	Selective expression of a subset of neuronal genes in oligodendroglioma with chromosome 1p loss.	Brain Pathology	14(1)	34-42	2004
Komura D, H. Nakamura, S. Tsutsumi, H. Aburatani and S. Ihara,	"Incorpolating prior Knowledge into clustering of gene expression profiles",	International Conference on Genome Informatics,	15	P036 1- 2	2004
Minamino, T., Miyauchi, H., Yoshida, T., Tateno, K., Komuro, I.	The role of vascular cell senescence in atherosclerosis: antisenescence as a novel therapeutic strategy for vascular aging.	Curr Vasc Pharmaco	12	141-148	2004
Ohtsuka,M., Takano, H., Suzuki, M., Zou, Y., Akazawa, H., Tamagawa, M., Wakimoto, K., Nakaya, H., Komuro, I.	Role of Na^+-Ca^{2+} exchanger in myocardial ischemia/reperfusion injury: evaluation using a heterozygous Na^+-Ca^{2+} exchanger knockout mouse model.	Biochem Biophys Res Commun	314	849-853	2004
Maraganore DM, Lesnick TG, Elbaz A, Chartier-Harlin M-C, Gasser T, Kr灰er R, Hattori N, Mellick GD, Quattrone A, Satoh J, Toda T, Wang J, Ioannidis JPA, de Andrade M, Rocca WA, the UCHL1 Global Genetics Consortium.	UCHL1 is a Parkinson¬s disease susceptibility gene.	Ann Neurol	55	512-521	2004
Popiel HA, Nagai Y, Onodera O, Inui T, Fujikake N, Urade Y, Strittmatter WJ, Burke JR, Ichikawa A, Toda T.	Disruption of the toxic conformation of the expanded polyglutamine stretch leads to suppression of aggregate formation and cytotoxicity.	Biochem Biophys Res Commun	317	1200-1206	2004
Akasaka-Manya K, Manya H, Kobayashi K, Toda T, Endo T.	Structure-function analysis of human protein O-linked mannose b1,2-N-acetylglucosaminyltransferase 1, POMGnT1.	Biochem Biophys Res Commun	320	39-44	2004

Longman C, Mercuri E, Cowan F, Allsop J, Brockington M, Jimenez-Mallebrera C, Kumar S, Rutherford M, Toda T, Muntoni F.	Antenatal and postnatal brain magnetic resonance imaging in muscle-eye-brain disease.	Arch Neurol	61	1301-1306	2004
Kurahashi H, Inagaki H, Yamada K, Ohye T, Taniguchi M, Emanuel B S, Toda T.	Cruciform DNA structure underlies the etiology for palindrome-mediated human chromosomal translocations.	J Biol Chem	279	35377-35383	2004
Hatano Y, Li Y, Sato K, Asakawa S, Yamamura Y, Tomiyama H, Yoshino H, Asahina M, Kobayashi S, Hassin-Baer S, Lu CS, Ng AR, Rosales RL, Shimizu N, Toda T, Mizuno Y, Hattori N.	Novel PINK1 mutations in early-onset parkinsonism.	Ann Neurol	56	424-427	2004
Ohtake H, Limprasert P, Fan Y, Onodera O, Kakita A, Takahashi H, Bonner LT, Tsuang DW, Murray I V, Lee VM, Trojanowski JQ, Ishikawa A, Idezuka J, Murata M, Toda T, Bird TD, Leverenz JB, Tsuji S, La Spada AR.	b-synuclein gene alteratio ns in dementia with Lewy bodies.	Neurology	63	805-811	2004

Hatano Y, Sato K, Eibol B, Yoshino H, Yamamura Y, Bonifati V, Shinotoh H, Asahina M, Kobayashi S, Ng AR, Rosales RL, Hassin-Baer S, Shinar Y, Lu CS, Chang HC, Wu-Chou YH, Atac FB, Kobayashi T, Toda T, Mizuno Y, Hattori N.	PARK6-linked autosomal recessive early-onset parkinsonism in Asian populations.	Neurology	63	1482-1485	2004
Kariya S, Hirano M, Nagai Y, Furiya Y, Fujikake N, Toda T, Ueno S.	Humanin attenuates apoptosis induced by DRPLA proteins with expanded polyglutamine stretches.	J Mol Neurosci			in press
Kurahashi H, Taniguchi M, Meno C, Taniguchi Y, Takeda S, Horie M, Otani H, Toda T.	Basement membrane fragility underlies embryonic lethality in fukutin-null mice.	Neurobiol Dis			in press
Li Y, Tomiyama H, Sato K, Hatano Y, Yoshino H, Atsumi M, Kitaguchi M, Sasaki S, Kawaguchi S, Miyajima H, Toda T, Mizuno Y, Hattori N.	Clinicogenetic study of PINK1 mutations in autosomal recessive early-onset parkinsonism.	Neurology			in press
Moroi Y, Yu B, Urabe K, Koga T, Nakahara T, Dainichi T, Uchi H, Furue M.	Effects of MAPK inhibitors on CCR4-mediated chemotaxis against thymus and activation-regulated chemokine (TARC/CCL17).	J Dermatol Sci.	36	186-8	2004
Nakahara T, Koga T, Fukagawa S, Uchi H, Furue M.	Intermittent topical corticosteroid/ tacrolimus sequential therapy improves lichenification and chronic papules more efficiently than intermittent topical corticosteroid/emollient sequential therapy in patients with atopic dermatitis.	J Dermatol	31	524-8	2004

Nakahara T, Uchi H, Urabe K, Chen Q, Furue M, Mor oi Y.	Role of c-Jun N-terminal kinase on lipopolysacch aride induced maturation of human monocyte-deri ved dendritic cells.	Int Immunol.	16	1701-9	2004
Nakazono-Kusaba A, Takahashi-Yana ga F, Miwa Y, M orimoto S, Furue M, Sasaguri T.	PKC412 induces apoptosi s through a caspase-depe ndent mechanism in hum an keloid-derived fibrobl asts.	Eur J Pharmac ol.	497	155-60	2004
Zhang M, Ishii K, Hisaeda H, Murat a S, Chiba T, Tan aka K, Li Y, Obat a C, Furue M, Hi meno K.	Ubiquitin-fusion degradati on pathway plays an ind ispensable role in naked DNA vaccination with a chimeric gene encoding a syngeneic cytotoxic T lymphocyte epitope of melanocyte and green flu orescent protein.	Immunology	112	567-74	2004
Moroi Y, Fujita S, Fukagawa S, Mas hino T, Goto T, Masuda T, Urabe K, Kubo K, Matsu i H, Kagawa S, K uroyanagi Y, Furu e M.	Clinical evaluation of all ogeneic cultured dermal substitutes for intractable skin ulcers after tumor r esection.	Eur J Dermato l	14	172-6	2004
Furue M, Terao H, Moroi Y, Koga T, Kubota Y, Na kayama J, Furuka wa F, Tanaka Y, Katayama I, Kinuk awa N, Nose Y, Urabe K.	Dosage and adverse effe cts of topical tacrolimus and steroids in daily ma nagement of atopic derm atitis.	J Dermatol.	31	277-83	2004
Masuda T, Furue M, Matsuda T.	Photocured, styrenated ge latin-based microspheres for de novo adipogenesis through corelease of ba sic fibroblast growth fact or, insulin, and insulin-li ke growth factor I.	Tissue Eng	10	523-35	2004
Obata C, Zhang M, Moroi Y, Hisa eda H, Tanaka K, Murata S, Furue M, Himeno K.	Formalin-fixed tumor cell s effectively induce antit umor immunity both in prophylactic and therapeu tic conditions.	J Dermatol Sc i.	34	209-19	2004

Fujii-Maeda S, Kajiwara K, Ikizawa K, Shinazawa M, Yu B, Koga T, Furue M, Yanagihara Y.	Reciprocal regulation of thymus and activation-regulated chemokine/macrophage-derived chemokine production by interleukin (IL)-4/IL-13 and interferon-gamma in HaCaT keratinocytes is mediated by alternations in E-cadherin distribution.	J Invest Dermatol	122	20-8	2004
Masuda T, Furue M, Matsuda T.	Novel strategy for soft tissue augmentation based on transplantation of fragmented omentum and preadipocytes.	Tissue Eng	10	1672-83	2004
Minami, T, Horiuchi, K., Miura, M., Abid, R., Takabe, W., Kohro, T., Ge, X., Aburatani, H., Hamakubo, T., Kodama, T., and Aird, W.C.	VEGF- and thrombin-induced termination factor, down syndrome critical region-1, attenuates endothelial cell proliferation and angiogenesis	J Biol Chem.	279	50537-54	2004
Minami, T., Murakami, T., Horiuchi, K., Miura, M., Noguchi, T., Miyazaki, J.I., Hamakubo, T., Aird, W.C., and Kodama,T.	Interaction between Hex and GATA transcription factors in vascular endothelial cells inhibits flk-1/KDR-mediated VEGF signaling.	J. Biol. Chem.	279	20626-35	2004
Minami, T., Sugiyama, A., Wu, SQ., Abid, R., Kodama, T., and Aird, W.C.	Thrombin and Phenotype Modulation of the Endothelium.	Arterioscler. Thromb. Vasc. Biol.	24	41-53	2004

ORIGINAL PAPER

Vol. 21 no. 4 2005, pages 439–444
doi:10.1093/bioinformatics/bti188

Multidimensional support vector machines for visualization of gene expression data

D. Komura [1,*], H. Nakamura[1], S. Tsutsumi[1], H. Aburatani[2] and S. Ihara[1]

[1]Research Center for Advanced Science and Technology and [2]Genome Science Division, Center for Collaborative Research, University of Tokyo, Tokyo 153-8904, Japan

Received on May 21, 2004; accepted on November 11, 2004
Advance Access publication December 17, 2004

ABSTRACT

Motivation: Since DNA microarray experiments provide us with huge amount of gene expression data, they should be analyzed with statistical methods to extract the meanings of experimental results. Some dimensionality reduction methods such as Principal Component Analysis (PCA) are used to roughly visualize the distribution of high dimensional gene expression data. However, in the case of binary classification of gene expression data, PCA does not utilize class information when choosing axes. Thus clearly separable data in the original space may not be so in the reduced space used in PCA.

Results: For visualization and class prediction of gene expression data, we have developed a new SVM-based method called multidimensional SVMs, that generate multiple orthogonal axes. This method projects high dimensional data into lower dimensional space to exhibit properties of the data clearly and to visualize a distribution of the data roughly. Furthermore, the multiple axes can be used for class prediction. The basic properties of conventional SVMs are retained in our method: solutions of mathematical programming are sparse, and nonlinear classification is implemented implicitly through the use of kernel functions. The application of our method to the experimentally obtained gene expression datasets for patients' samples indicates that our algorithm is efficient and useful for visualization and class prediction.

Contact: komura@hal.rcast.u-tokyo.ac.jp

1 INTRODUCTION

DNA microarray has been the key technology in modern biology and helped us to decipher the biological system because of its ability to monitor the expression levels of thousands of genes simultaneously. Since DNA microarray experiments provide us with huge amount of gene expression data, they should be analyzed with statistical methods to extract the meanings of experimental results.

A great number of supervised learning algorithms have been proposed and applied to classification of gene expression data (Golub *et al.*, 1999; Tibshirani *et al.*, 2002; Khan *et al.*, 2001). Support Vector Machines (SVMs) have been paid attention in recent years because of their good performance in various fields, especially in the area of bioinformatics including classification of gene expression data (Furey *et al.*, 2000). However, SVMs predict a class of test samples by projecting the data into one-dimensional space based on a decision function. As a result, information loss of the original data is enormous.

Some methods are used for projecting high dimensional data into lower dimensional space to clearly exhibit the properties of the data and to roughly visualize the distribution of the data. Principal Component Analysis (PCA) (Fukunaga, 1990) and its derivatives, e.g. Nonlinear PCA (Diamantaras and Kung, 1996) and Kernel PCA (Schölkopf *et al.*, 1998), are most widely used for this purpose (Huang *et al.*, 2003). One drawback of PCA analysis is, however, that class information is not utilized for class prediction because PCA chooses axes based on the variance of overall data. Thus clearly separable data in the original space may not be so in the reduced space used in PCA. Another method for visualization and reducing dimension of data is discriminant analysis. It chooses axes based on class information in terms of within- and between-class variance. However, it is reported that SVMs often outperform discriminant analysis (Brown *et al.*, 2000).

The main purpose of this paper is to cover the shortcoming of SVMs by introducing multiple orthogonal axes for reducing dimensions and visualization of gene expression data. To this end, we have developed multidimensional SVMs (MD-SVMs), a new SVM-based method that generates multiple orthogonal axes based on margin between two

*To whom correspondence should be addressed.

Komura *et al.* (2004) Multidimensional Support Vector Machines for Visualization of Gene Expression Data. Symposium on Applied Computing, Proceedings of the 2004 ACM symposium on Applied computing, 175-179; http://doi.acm.org/10.1145/967900.967936

classes to minimize generalization errors. The axes generated by this method reduce dimensions of original data to extract information useful in estimating the discriminability of two classes. This method fulfills the requirement of both visualization and class prediction. The basic properties of SVMs are retained in our method: solutions of mathematical programming are sparse, and nonlinear classification of data is implemented implicitly through the use of kernel functions.

This paper is organized as follows. In Section 2, we introduce the fundamental of SVMs. In Section 3, we describe the algorithm of MD-SVMs. In Section 4 and 5, we show numerical experiments on real gene expression datasets and reveal that our algorithm is effective for data visualization and class prediction.

1.1 Notation

$\mathbb{R}$ is defined as the set of real numbers. Each component of a vector $\boldsymbol{x} \in \mathbb{R}^n, i = 1,\ldots,m$ will be denoted by $x_j, j = 1,\ldots,n$. The inner product of two vectors $\boldsymbol{x} \in \mathbb{R}^n$ and $\boldsymbol{y} \in \mathbb{R}^n$ will be denoted by $\boldsymbol{x} \cdot \boldsymbol{y}$. For a vector $\boldsymbol{x} \in \mathbb{R}^n$ and a scalar $a \in \mathbb{R}, a \leq \boldsymbol{x}$ is defined as $a \leq x_i$ for all $i = 1,\ldots,n$. For an arbitrary variable x, x^k is just a name of the variable with upper suffix, not defined as k-th power of x.

2 SUPPORT VECTOR MACHINES

Since details of SVMs are fully described in the articles (Vapnik, 1998; Cristianini and Shawe-Taylor, 2000), we briefly introduce the fundamental principle of SVMs in this section. We consider a binary classification problem, where a linear decision function is employed to separate two classes of data based on m training samples $\boldsymbol{x}_i \in \mathbb{R}^n, i = 1,\ldots,m$ with corresponding class values $y_i \in \{\pm 1\}, i = 1,\ldots,m$. SVMs map a data $\boldsymbol{x} \in \mathbb{R}^n$ into a higher, probably infinite, dimensional space $\mathbb{R}^N$ than the original space with an appropriate nonlinear mapping $\phi : \mathbb{R}^n \to \mathbb{R}^N, n < N$. They generate the linear decision function of the form $f(\boldsymbol{x}) = \mathrm{sign}(\boldsymbol{w} \cdot \phi(\boldsymbol{x}) + b)$ in the high dimensional space, where $\boldsymbol{w} \in \mathbb{R}^N$ is a weight vector which defines a direction perpendicular to the hyperplane of the decision function, while $b \in \mathbb{R}$ is a bias which moves the hyperplane parallel to itself. The optimal decision function given by SVMs is a solution of an optimization problem

$$\min_{w,\xi} \frac{1}{2}\|w\|^2 + C\sum_{i=1}^{m}\xi_i,$$

$$\text{s.t. } y_i(\boldsymbol{w} \cdot \phi(\boldsymbol{x}_i) + b) \geq 1 - \xi_i, \quad i = 1,\ldots,m, \xi \geq 0, \quad (1)$$

with $C > 0$. Here, $\xi \in \mathbb{R}^m$ is a vector whose elements are slack variables and $C \in \mathbb{R}$ is a regularization parameter for penalizing training errors. When $C \to \infty$, no training errors are allowed, and thus this is called hard margin classification. When $0 < C < \infty$, this is called soft margin classification because it allows some training errors. Note that a geometric margin γ between two classes is defined as $\frac{1}{\|w\|^2}$. The optimization problem formalizes the tradeoff between maximizing margin and minimizing training errors. The problem is transformed into its corresponding dual problem by introducing lagrange multiplier $\boldsymbol{\alpha} \in \mathbb{R}^m$ and replacing $\phi(\boldsymbol{x}_i) \cdot \phi(\boldsymbol{x}_j)$ by kernel function $K(\boldsymbol{x}_i, \boldsymbol{x}_j) = \phi(\boldsymbol{x}_i) \cdot \phi(\boldsymbol{x}_j)$ to be solved in an elegant way of dealing with a high dimensional vector space. The dual problem is

$$\max_{\alpha} -\frac{1}{2}\sum_{i=1}^{m}\sum_{j=1}^{m}\alpha_i\alpha_j y_i y_j K(\boldsymbol{x}_i, \boldsymbol{x}_j) + \sum_{i=1}^{m}\alpha_i,$$

$$\text{s.t. } 0 \leq \boldsymbol{\alpha} \leq C, \sum_{i=1}^{m}\alpha_i y_i = 0. \quad (2)$$

By virtue of the kernel function, the value of the inner product $\phi(\boldsymbol{x}_i) \cdot \phi(\boldsymbol{x}_j)$ can be obtained without explicit calculation of $\phi(\boldsymbol{x}_i)$ and $\phi(\boldsymbol{x}_j)$. Finally, the decision function becomes $f(\boldsymbol{x}) = \mathrm{sign}\left(\sum_{i=1}^{m}\alpha_i y_i K(\boldsymbol{x}_i, \boldsymbol{x}) + b\right)$. by using kernel functions between training samples $\boldsymbol{x}_i, i = 1,\ldots,m$ and a test sample $\boldsymbol{x}$.

3 MULTIDIMENSIONAL SUPPORT VECTOR MACHINES

In order to overcome the drawback that SVMs cannot generate more than one decision function, we propose a SVM-based method that can be used for both data visualization and class prediction in this section. We call this method multidimensional SVMs (MD-SVMs). We deal with the same problem as mentioned in Section 2. Conventional SVMs give an optimal solution set $(\boldsymbol{w}, b, \boldsymbol{\xi})$ which corresponds to a decision function, while our MD-SVMs give the multiple sets $(\boldsymbol{w}^k, b^k, \boldsymbol{\xi}^k), k = 1,2,\ldots,l$ with $l \leq n$, so that all the directions $\boldsymbol{w}_k$ are orthogonal to one another. The orthogonal axes can be used for reducing the dimension of original data and data visualization in three dimensional space by means of projection. Here the first set $(\boldsymbol{w}^1, b^1, \boldsymbol{\xi}^1)$ is equivalent to that obtained by conventional SVMs. Now we only refer to the steps of obtaining $(\boldsymbol{w}^k, b^k, \boldsymbol{\xi}^k), k = 2,3,\ldots,l$. In practice, the k-th set $(\boldsymbol{w}^k, b^k, \boldsymbol{\xi}^k) k = 2,3,\ldots,l$ are found with iterative computations of the optimization problem

$$\min_{\boldsymbol{w}^k,\boldsymbol{\xi}^k} \frac{1}{2}\|\boldsymbol{w}^k\|^2 + C\sum_{i=1}^{m}\xi_i^k,$$

$$\text{s.t. } y_i(\boldsymbol{w}^k \cdot \phi(\boldsymbol{x}_i) + b^k) \geq 1 - \xi_i^k, i = 1,\ldots,m,$$

$$\boldsymbol{\xi}^k \geq 0, \boldsymbol{w}^k \cdot \boldsymbol{w}^j = 0, j = 1,\ldots,k-1. \quad (3)$$

This problem differs from that of conventional SVMs in the last constraint $\boldsymbol{w}^k \cdot \boldsymbol{w}^j = 0$. The weight vector $\boldsymbol{w}^j, j = 1,\ldots,k-1$ should be computed in advance by solving

other optimization problems (3). The optimization problem is modified by introducing lagrange multipliers $\alpha^k, \gamma^k \in \mathbb{R}^m$, $\beta^k \in \mathbb{R}^{k-1}$ and kernel functions. The primal Lagrangian is

$$L(w^k, b^k, \xi^k) = \frac{1}{2}\| w^k \|^2 + C\sum_{i=1}^{m} \xi_i^k + \sum_{i=1}^{m} \alpha_i^k (1 - \xi_i^k - y_i(w^k \cdot \phi(x_i) + b^k)) + \sum_{j=1}^{k-1} \beta_j^k (w^k \cdot w^j) - \sum_{i=1}^{m} \gamma_i^k \xi_i. \quad (4)$$

Consequently, the optimization problem is

$$\max_{\alpha^k, \beta^k} -\frac{1}{2}\sum_{i=1}^{m}\sum_{j=1}^{m} \alpha_i^k \alpha_j^k y_i y_j K(x_i, x_j) + \frac{1}{2}\sum_{i=1}^{k-1} \beta_i^k \beta_i^k (w^i \cdot w^i) + \sum_{i=1}^{m} \alpha_i^k,$$

$$\text{s.t. } 0 \le \alpha^k \le C, \sum_{i=1}^{m} \alpha_i^k y_i = 0,$$

$$\sum_{i=1}^{m} \alpha_i^k y_i (\phi(x_i) \cdot w^j) = 0, j = 1, \ldots, k-1 \quad (5)$$

Here $\phi(x_p) \cdot w^q$ and $w^p \cdot w^p$ are calculated recursively as follows:

$$\phi(x_p) \cdot w^q = \sum_{i=1}^{m} \alpha_i^q y_i K(x_p, x_i) - \sum_{i=1}^{q-1} \beta_i^q (\phi(x_p) \cdot w^i), \quad (6)$$

$$w^p \cdot w^p = \sum_{i=1}^{m}\sum_{j=1}^{m} \alpha_i^p \alpha_j^p y_i y_j K(x_i, x_j) - \sum_{i=1}^{m}\sum_{j=1}^{p-1} \alpha_i^p y_i \beta_j^p (\phi(x_i) \cdot w^j) + \sum_{i=1}^{p-1} \beta_i^p \beta_i^p (w^i \cdot w^i) - \sum_{i=1}^{m}\sum_{j=1}^{p-1} \alpha_i^p y_i \beta_j^p (\phi(x_i) \cdot w^j), \quad (7)$$

where $\phi(x_p) \cdot w^1 = \sum_{i=1}^{m} \alpha_i^1 y_i K(x_p, x_i)$ and $w^1.w^1 = \sum_{i=1}^{m} \alpha_i^1 y_i (\phi(x_i), w^1)$. As can be seen, there is no need to calculate nonlinear map of data $\phi(x)$ in problem (5) because all nonlinear mappings can be replaced with kernel functions.

Note that this optimization problem is a nonconvex quadratic problem when k is more than 1. As a consequence, the optimal solutions are not easy to be obtained. In Section 4, we use local optimum for numerical experiments when k is 2 or 3. We note the experimental results are still encouraging.

The corresponding Karush–Kuhn–Tucker conditions are

$$\alpha_i^k \{1 - \xi_i^k - y_i(w^k \cdot \phi(x_i) + b^k)\} = 0, \quad (8)$$

$$\xi_i^k (\alpha_i^k - C) = 0, i = 1, \ldots, m. \quad (9)$$

These are exactly the same as conventional SVMs. We highlight the other properties conserved from conventional SVMs:

- Projecting data into high dimensional space is implicit, using kernel functions to replace inner products.
- The solutions α^k of the optimization problem is sparse. Then the corresponding decision function depends only on few 'Support Vectors'.

Since each decision function is normalized independently to hold $w^k \cdot \phi(x_i) + b^k = y_i$ for $i = 1, \ldots, m$, data scales of the axes should be aligned with first axis ($k = 1$) for visualization. The margin γ^k, the L2-distance between support vectors of each class of k-th axis, is

$$\left(\sum_{i=1}^{m}\sum_{j=1}^{m} \alpha_i^k \alpha_j^k y_i y_j K(x_i, x_j) - \sum_{i=1}^{k-1} \beta_i^k \beta_i^k (w^i \cdot w^i) \right)^{-\frac{1}{2}} \quad (10)$$

So a scaling factor $s^k = \gamma^1 / \gamma^k$ is

$$\sqrt{\frac{\sum_{i=1}^{m}\sum_{j=1}^{m} \alpha_i^1 \alpha_j^1 y_i y_j K(x_i, x_j)}{\sum_{i=1}^{m}\sum_{j=1}^{m} \alpha_i^k \alpha_j^k y_i y_j K(x_i, x_j) - \sum_{i=1}^{k-1} \beta_i^k \beta_i^k (w^i \cdot w^i)}}. \quad (11)$$

The decision function of k-th step has the form $f^k(x) = \text{sign}\left(\sum_{i=1}^{m} \alpha_i^k y_i K(x_i, x) + b^k\right)$. Since the right hand side of the equation has the function of projecting original data into one dimensional space, the data can be plot in up to three dimensional space for visualization. The coordinate of data $x \in \mathbb{R}^m$ in three dimensional space is

$$(s^{k_1} g^{k_1}(x), s^{k_2} g^{k_2}(x), s^{k_3} g^{k_3}(x)), \quad (12)$$

where $g^k(x) = \sum_{i=1}^{m} \alpha_i^k y_i K(x_i, x) + b^k$. The space represents a distribution of data clearly based on the margin between two classes.

4 NUMERICAL EXPERIMENTS

4.1 Method

In order to confirm the effectiveness of our algorithm, we have performed numerical experiments. MD-SVMs can generate multiple axes, up to the number of features. Here we choose three axes, $k = 1, 2, 3$, to simplify the experiments. When k is

2 or 3, we use local optimum in problem (5) since it is difficult to obtain the global solutions. In our experiments, we carry out hold-out validation because cross-validation changes decision functions every time the dataset is split. Then we compare the results obtained by MD-SVMs with those obtained by PCA.

In the experiments, the expression values for each of the genes are normalized such that the distribution over the samples has a zero mean and unit variance. Before normalization, we discard genes in the dataset with the overall average value less than 0.35. Then we calculate a score $F(x(j)) = |(\mu^+(j)-\mu^-(j))/(\sigma^+(j)+\sigma^-(j))|$, for the remaining genes. Here $\mu^+(j)(\mu^-(j))$ and $\sigma^+(j)(\sigma^-(j))$ denote the mean and standard deviation of the j-th gene of the samples labeled $+1(-1)$, respectively. This score becomes the highest when the corresponding expression levels of the gene differ most in the two classes and have small deviations in each class. We select 100 genes with the highest scores and use them for hold-out validation. These procedures for gene selection are done only for training data for fair experiments.

The regularization parameter C in problem (5) is set to 1000. This value is rather large but finite because we would like to avoid ill-posed problems in a hard margin classification. We choose linear kernel $K(\boldsymbol{x}_i,\boldsymbol{x}_j) = \boldsymbol{x}_i \cdot \boldsymbol{x}_j$ and RBF kernel $K(\boldsymbol{x}_i,\boldsymbol{x}_j) = \exp -\gamma \|\boldsymbol{x}_i - \boldsymbol{x}_j\|^2$ with $\gamma = 0.001$ in the experiments of MD-SVMs.

4.2 Materials

Leukemia dataset (Golub et al., 1999) This gene expression dataset consists of 72 leukemia samples, including 25 acute myeloid leukemia (AML) samples and 47 acute lymphoblastic leukemia (ALL) samples. They are obtained by hybridization on the Affymetrix GeneChip containing probe sets for 7070 genes. Training set contains 20 AML samples and 42 ALL samples. Test set contains 5 AML samples and 5 ALL samples. AML samples are labeled $+1$ and ALL samples are labeled -1.

Lung tissue dataset (Bhattacharjee et al., 2001) This dataset consists of 203 samples from lung tissue, including 16 samples from normal tissue and 187 samples from cancerous tissue, and is obtained by hybridization on the Affymetrix U95A Genechip containing probe sets for 12558 genes. Training set includes 13 samples from normal tissue and 157 samples from cancerous tissue. Test set includes 3 samples from normal tissue and 30 samples from cancerous tissue. Samples from normal tissue are labeled $+1$ and samples from cancerous tissue are labeled -1.

5 RESULTS AND DISCUSSION

The results of numerical experiments are shown in Figure 1, and Tables 1 and 2. The distributions obtained by MD-SVMs on the leukemia dataset and the lung tissues dataset are given in Figure 1-(1) and 1-(3), respectively. Those obtained by PCA are given in Figure 1-(2) and 1-(4), respectively. The number of misclassified samples by MD-SVMs are summarized in Table 1 and 2. In these tables, the class of the samples is predicted based on decision functions $f^k(\boldsymbol{x}), k = 1,2,3$, corresponding to each of the three axes.

Figure 1-(1) and 1-(3) illustrate that MD-SVMs are likely to separate the samples of each class in all the three directions. However, as shown in Figure 1-(2) and 1-(4), PCA does not separate the samples in the directions of the 2nd or the 3rd axis. These axes by PCA are dispensable with the objective of visualization for class prediction. In other words, MD-SVMs gather the plots of the samples into the appropriate clusters of each class, while PCA rather scatters them. Furthermore, in the distribution by MD-SVMs for the lung tissues dataset, one sample outlies from correct clusters (indicated by arrows in Figure 1-(3)). Though this sample also seems to be an outlier in the distribution by PCA (also indicated in Figure 1-(4)), the outlier significantly deviates in MD-SVMs. This may arise from the fact that MD-SVMs can separate the samples in all the directions. These observations indicate that MD-SVMs are well suited for visualizing in binary classification problems.

The significant advantage of MD-SVMs over PCA is the ability to predict the classes. MD-SVMs can predict the classes of samples based on the decision functions $f^k(\boldsymbol{x})$ without extra computation, while PCA cannot. The predicted class of a sample should be matched by the all the decision functions in an ideal case. However that does not always occur as seen in Tables 1 and 2. In such cases, the simplest method for prediction is to use only the 1st axis, which corresponds to the decision function generated by conventional SVMs. The idea is supported by the fact that the 1st decision function classifies the samples most correctly in almost all cases in Tables 1 and 2. The more advanced method is weighted voting. Scaling factor or normalized objective values in problem (5) are the candidate of the weight.

Multiple decision functions generated by MD-SVMs are useful for outlier detection. Samples misclassified by multiple decision functions may be mis-labeled or categorized into unknown classes. For example, see the column '3 axes' of test sample of the lung tissues dataset with RBF kernel in Table 2. This sample is misclassified by all decision functions, so we can say that this data contains some experimental error. The hierarchical clustering method also supports our result. These results indicate that MD-SVMs can be used for finding candidates of outliers.

6 CONCLUSION

For both visualization and class prediction of gene expression data, we propose a new method called Multidimensional Support Vector Machines. We formulate the method as a quadratic program and implement the algorithm. This is motivated by the following facts: (1) SVMs perform better than the other classification algorithms, but they generate only one axis for class prediction. (2) PCA chooses multiple

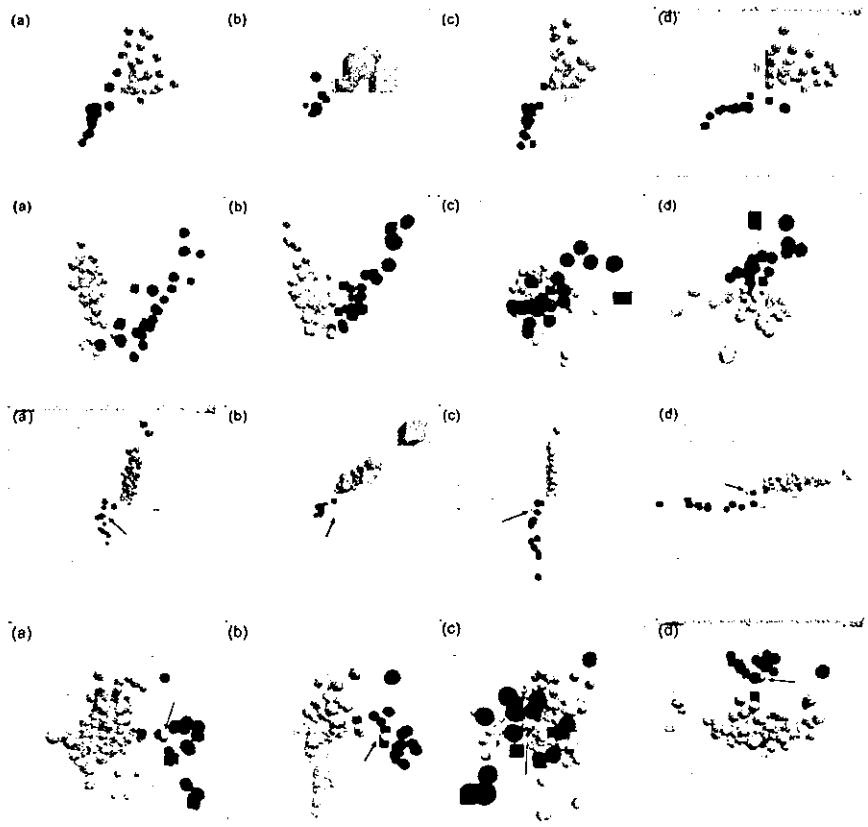

Fig. 1. (Top row) Distribution obtained by MD-SVMs for the leukemia dataset with linear kernel. (Second row) Distribution obtained by PCA on the leukemia dataset. (Third row) Distribution obtained by MD-SVMs for the lung tissues dataset with linear kernel. The sample indicated by arrows appears to be an outlier. (Fourth row) Distribution obtained by PCA for the lung tissues dataset. The sample indicated by arrows is the same as in the third row but with less deviates. (a) Cross shot, (b) 1st axis (x axis) and 2nd axis (y axis), (c) 2nd axis (x axis) and 3rd axis (y axis), (d) 3rd axis (x axis) and 1st axis (y axis). Black objects and white objects indicate AML samples (or normal tissues) ALL samples (or cancreous tissues), respectively. Training data and test data are expressed as a sphere and a cube, respectively.

Table 1. Number of classification errors in the MD-SVMs for the leukemia dataset. The columns 'n-th axis', $n = 1, 2, 3$, indicates the number of samples misclassified by n-th decision function. The columns 'n axes', $n = 1, 2, 3$, indicates the number of samples misclassified by n decision functions

Kernel	Sample	# of samples	1st axis	2nd axis	3rd axis	1 axis	2 axes	3 axes
Linear	Training	62	0	1	2	1	1	0
RBF	Training	62	0	2	7	5	2	0
Linear	Test	10	1	1	2	2	1	0
RBF	Test	10	0	2	0	2	0	0

Table 2. Number of classification errors in the MD-SVMs on the lung dataset. See the caption of Table 1 for other explanation

Kernel	Sample	# of samples	1st axis	2nd axis	3rd axis	1 axis	2 axes	3 axes
Linear	Training	170	0	1	1	0	1	0
RBF	Training	170	0	3	5	2	3	0
Linear	Test	33	1	0	0	1	0	0
RBF	Test	33	1	1	1	0	0	1

orthogonal axes, but it cannot predict classes of samples without other classification algorithms. We have tried to cover the shortcomings of both methods. MD-SVMs choose multiple orthogonal axes, which correspond to decision functions, from high dimensional space based on a margin between two classes. These multiple axes can be used for both visualization and class prediction.

Numerical experiments on real gene expression data indicate the effectiveness of MD-SVMs. All axes generated by MD-SVMs are taken into account for separating class of samples, while the 2nd and the 3rd axes by PCA are not. The samples in the distributions by MD-SVMs gather into appropriate clusters more vividly than those by PCA. MD-SVMs can predict the classes of the samples with multiple decision functions. We also indicate that MD-SVMs are useful for outlier detection with multiple decision functions.

There are several future works to be done on MD-SVMs: (1) application of our method to wider variety of gene expression datasets, (2) investigation of gene selection for preprocess of analysis and (3) investigation on class prediction method with multiple decision functions. Firstly, the use of more suitable samples may show that the axes chosen by MD-SVMs separate samples more clearly than those by PCA. Secondly, since the conventional SVMs show good generalization performance especially with large number of features, it is expected that MD-SVMs show much better performance than PCA with increasing the number of genes used in the numerical experiments. Since the element of weight vector generated by SVMs is one of the measures of discrimination power of the corresponding genes (Guyon *et al.*, 2002), that generated by MD-SVMs can be used for gene selection. Thirdly, the classification with probability as well as the weighted voting mentioned in Section 4 may be achieved in our scheme since the conventional SVMs have been already expanded for the purpose with sigmoid functions (Platt, 1999). We hope that our method sheds some lights on the future study of gene expression experiments.

REFERENCES

Bhattacharjee,A., Richards,W., Staunton,J., Li,C., Monti,S., Vasa,P., Ladd,C., Beheshti,J., Bueno,R., Gillette,M. *et al.* (2001) Classification of human lung carcinomas by mRNA expression profiling reveals distinct adenocarcinoma subclasses. *Proc. Natl Acad. Sci. USA*, **98**, 13790–13795.

Brown,M., Grundy,W., Lin,D., Cristianini,N., Sugnet,C., Furey,T., Ares,M. and Haussler,D. (2000) Knowledge-based analysis of microarray gene expression data by using support vector machines. *Proc. Natl Acad. Sci. USA*, **97**, 262–267.

Cristianini,N. and Shawe-Taylor,J. (2000) *An Introduction to Support Vector Machines and Other Kernel-based Learning Methods*. Cambridge University Press, NY.

Diamantaras,K. and Kung,S. (1996) *Principal Component Neural Networks Theory and Applications*. John Wiley & Sons, NY.

Fukunaga,K. (1990) *Introduction to Statistical Pattern Recognition*. Academic Press, NY.

Furey,T., Cristianini,N., Duffy,N., Bednarski,D., Schummer,M. and Haussler,D. (2000) Support vector machine classification and validation of cancer tissue samples using microarray expression data. *Bioinformatics*, **16**, 906–914.

Golub,T., Slonim,D., Tamayo,P., Huard,C., Gaasenbeek,M., Mesirov,J., Coller,H., Loh,M., Downing,J., Caligiuri,M., Bloomfield,C. and Lander,E. (1999) Molecular classification of cancer: class discovery and class prediction by gene expression monitoring. *Science*, **286**, 531–537.

Guyon,I., Weston,J., Barnhill,S. and Vapnik,V. (2002) Gene selection for cancer classification using support vector machines. *J. Machine Learn.*, **46**, 389–422.

Huang,E., Ishida,S., Pittman,J., Dressman,H., Bild,A., Kloos,M., D'Amico,M., Pestell,R., West,M. and Nevins,J. (2003) Gene expression phenotypic models that predict the activity of oncogenic pathways. *Nat. Genet.*, **34**, 226–230.

Khan,J., Wei,J., Ringnér,M., Saal,L., Ladanyi,M., Westermann,F., Berthold,F., Schwab,M., Antonescu,C., Peterson,C. and Meltzer,P. (2001) Classification and diagnostic prediction of cancers using gene expression profiling and artificial neural networks. *Nat. Med.*, **7**, 673–679.

Platt,J. (1999) *Probabilistic Outputs for Support Vector Machines and Comparisons to Regularized Likelihood Methods*. MIT Press, Cambridge, MA.

Schölkopf,B., Smola,A. and Müller,K. (1998) Non-linear component analysis as a kernel eigenvalue problem. *Neural Comput.*, **10**, 1299–1319.

Tibshirani,R., Hastie,T., Narasimhan,B. and Chu,G. (2002) Diagnosis of multiple cancer types by shrunken centroids of gene expression. *Proc. Natl Acad. Sci. USA*, **99**, 6567–6572.

Vapnik,V. (1998) *Statistical Learning Theory*. John Wiley & Sons, NY.

nature medicine

G-CSF prevents cardiac remodeling after myocardial infarction by activating the Jak-Stat pathway in cardiomyocytes

Mutsuo Harada[1,4], Yingjie Qin[1,4], Hiroyuki Takano[1,4], Tohru Minamino[1,4], Yunzeng Zou[1], Haruhiro Toko[1], Masashi Ohtsuka[1], Katsuhisa Matsuura[1], Masanori Sano[1], Jun-ichiro Nishi[1], Koji Iwanaga[1], Hiroshi Akazawa[1], Takeshige Kunieda[1], Weidong Zhu[1], Hiroshi Hasegawa[1], Keita Kunisada[2], Toshio Nagai[1], Haruaki Nakaya[3], Keiko Yamauchi-Takihara[2] & Issei Komuro[1]

Granulocyte colony-stimulating factor (G-CSF) was reported to induce myocardial regeneration by promoting mobilization of bone marrow stem cells to the injured heart after myocardial infarction, but the precise mechanisms of the beneficial effects of G-CSF are not fully understood. Here we show that G-CSF acts directly on cardiomyocytes and promotes their survival after myocardial infarction. G-CSF receptor was expressed on cardiomyocytes and G-CSF activated the Jak/Stat pathway in cardiomyocytes. The G-CSF treatment did not affect initial infarct size at 3 d but improved cardiac function as early as 1 week after myocardial infarction. Moreover, the beneficial effects of G-CSF on cardiac function were reduced by delayed start of the treatment. G-CSF induced antiapoptotic proteins and inhibited apoptotic death of cardiomyocytes in the infarcted hearts. G-CSF also reduced apoptosis of endothelial cells and increased vascularization in the infarcted hearts, further protecting against ischemic injury. All these effects of G-CSF on infarcted hearts were abolished by overexpression of a dominant-negative mutant Stat3 protein in cardiomyocytes. These results suggest that G-CSF promotes survival of cardiac myocytes and prevents left ventricular remodeling after myocardial infarction through the functional communication between cardiomyocytes and noncardiomyocytes.

Myocardial infarction is the most common cause of cardiac morbidity and mortality in many countries, and left ventricular remodeling after myocardial infarction is important because it causes progression to heart failure. Several cytokines including G-CSF, erythropoietin and leukemia inhibitory factor have beneficial effects on cardiac remodeling after myocardial infarction[1–5]. In particular, G-CSF markedly improves cardiac function and reduce mortality after myocardial infarction in mice, possibly by regeneration of myocardium and angiogenesis[1,2,6–8]. G-CSF is known to have various functions such as induction of proliferation, survival and differentiation of hematopoietic cells, as well as mobilization of bone marrow cells[9–11]. Although it was reported that bone marrow cells could differentiate into cardiomyocytes and vascular cells, thereby contributing to regeneration of myocardium and angiogenesis in ischemic hearts[12–15], accumulating evidence has questioned these previous reports[16–18]. In this study, we examined the molecular mechanisms of how G-CSF prevents left ventricular remodeling after myocardial infarction.

RESULTS

G-CSF directly acts on cultured cardiomyocytes

G-CSF receptor (G-CSFR, encoded by *CSF3R*) has been reported to be expressed only on blood cells such as myeloid leukemic cells, leukemic cell lines, mature neutrophils, platelets, monocytes and some lymphoid cell lines[9]. To test whether G-CSFR is expressed on mouse cardiomyocytes, we performed a reverse transcription–polymerase chain reaction (RT-PCR) experiment by using specific primers for mouse *Csf3r*. We detected expression of the *Csf3r* gene in the adult mouse heart and cultured neonatal cardiomyocytes (**Fig. 1a**). We next examined expression of G-CSFR protein in cultured cardiomyocytes of neonatal rats by immunocytochemistry. Similar to the previously reported expression pattern of G-CSFR in living cells[19], the immunoreactivity for G-CSFR was localized to the cytoplasm and cell membrane under steady-state conditions in cardiomyocytes (**Fig. 1b**). This immunoreactivity disappeared when the antibody specific for G-CSFR was omitted, validating its specificity (**Fig. 1b**). In addition to cardiomyocytes, we also detected expression of G-CSFR on cardiac fibroblasts by immunocytochemistry (see **Supplementary Fig. 1** online) and RT-PCR (**Supplementary Fig. 2** online).

The binding of G-CSF to its receptor has been reported to evoke signal transduction by activating the receptor-associated Janus family tyrosine kinases (JAK) and signal transducer and activator of transcription (STAT) proteins in hematopoietic cells[9,10]. In particular, STAT3

[1]Department of Cardiovascular Science and Medicine, Chiba University Graduate School of Medicine, 1-8-1 Inohana, Chuo-ku, Chiba 260-8670, Japan. [2]Department of Molecular Medicine, Osaka University Medical School, Osaka University, 2-2 Yamadaoka, Suita, Osaka 565-0871, Japan. [3]Department of Pharmacology, Chiba University Graduate School of Medicine, 1-8-1 Inohana, Chuo-ku, Chiba 260-8670, Japan. [4]These authors contributed equally to this work. Correspondence should be addressed to I.K. (komuro-tky@umin.ac.jp).

Published online 20 February 2005; doi:10.1038/nm1199

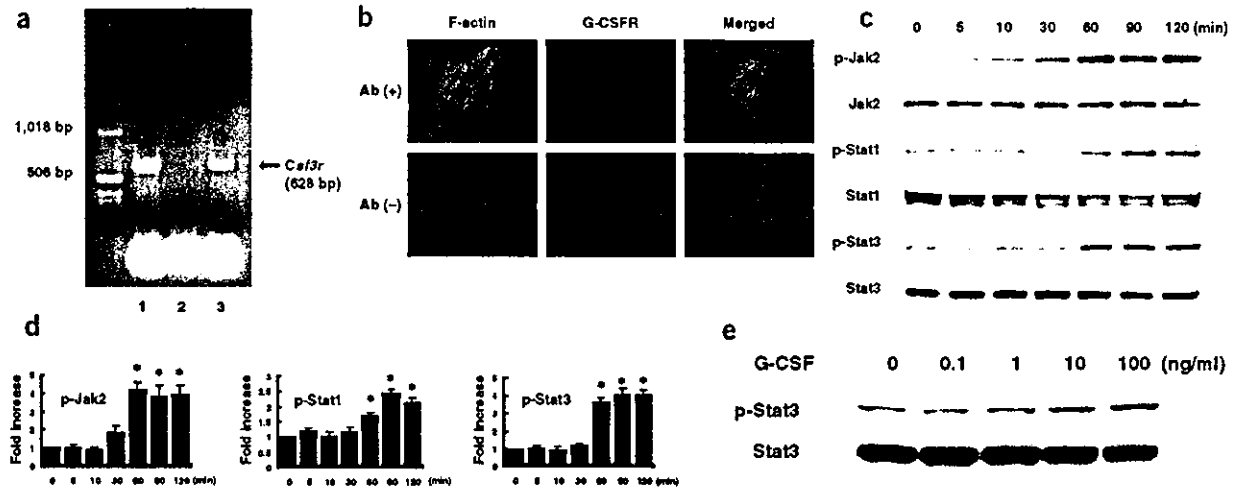

Figure 1 Expression of G-CSFR and the G-CSF-evoked signal transduction in cultured cardiomyocytes. (a) RT-PCR for mouse *Csf3r*. Expression of *Csf3r* was detected in the adult mouse heart (lane 1) and cultured cardiomyocytes of neonatal mice (lane 3). In lane 2, reverse transcription products were omitted to exclude the possibility of false-positive results from contamination. (b) Immunocytochemical staining for G-CSFR. Cardiomyocytes from neonatal rats were incubated with antibody to G-CSFR (red) and phalloidin (green) (upper panel). In the absence of antibody to G-CSFR, no signal was detected (lower panel). Original magnification, ×1,000. (c) G-CSF induces phosphorylation of Jak2, Stat1 and Stat3 in a time-dependent manner in cultured cardiomyocytes. (d) Quantification of Jak2, Stat1 and Stat3 activation by G-CSF stimulation as compared with control (time = 0). $^*P < 0.05$ versus control ($n = 3$). (e) G-CSF induces phosphorylation and activation of Stat3 in a dose-dependent manner in cultured cardiomyocytes.

has been reported to contribute to G-CSF-induced myeloid differentiation and survival[20,21]. We therefore examined whether G-CSF activates the Jak-Stat signaling pathway in cultured cardiomyocytes. G-CSF (100 ng/ml) significantly induced phosphorylation and activation of Jak2 and Stat3, and to a lesser extent, Stat1 but not Jak1, Tyk2 or Stat5 in a dose-dependent manner (Fig. 1c–e and data not shown), suggesting that G-CSFR on cardiomyocytes is functional.

We next examined whether G-CSF confers direct protective effects on cardiomyocytes as it prevents hematopoietic cells from apoptotic death[21]. We exposed cardiomyocytes to 0.1 mM H_2O_2 in the absence or presence of G-CSF and examined cardiomyocyte apoptosis by staining with annexin V[22,23]. Pretreatment with G-CSF significantly reduced the number of H_2O_2-induced annexin V–positive cells compared with cells that were not given the G-CSF pretreatment

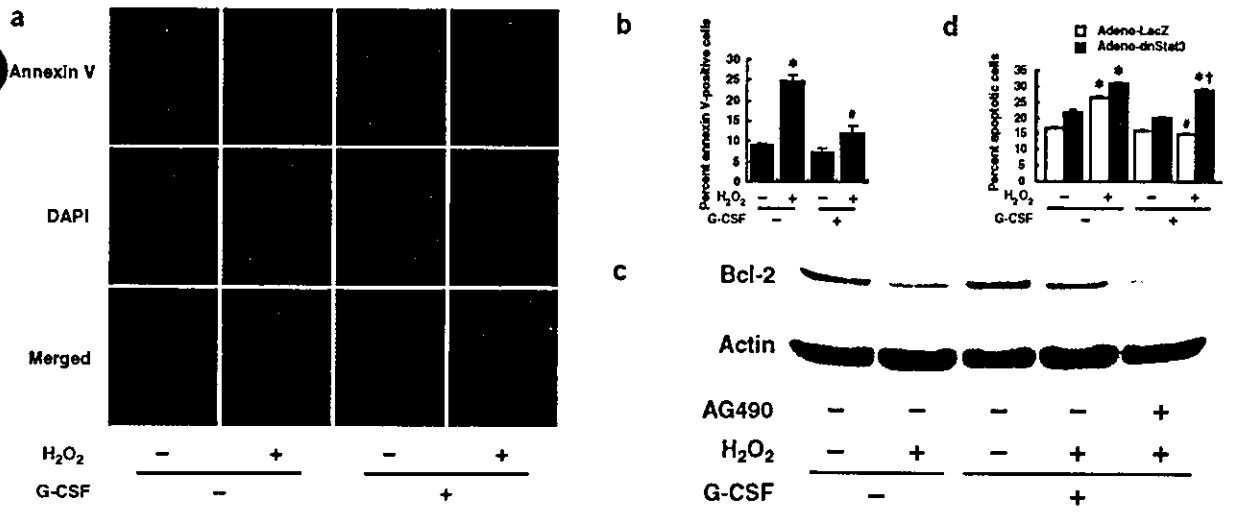

Figure 2 Suppression of H_2O_2-induced cardiomyocyte apoptosis by G-CSF. (a) Detection of apoptosis by Cy3-labeled annexin V. Red fluorescence shows apoptotic cardiomyocytes stained with Cy3-labeled annexin V. Nuclei were counterstained with DAPI staining (blue). Original magnification, ×400. (b) Quantitative analysis of apoptotic cells. The vertical axis indicates the ratio of the annexin V–positive cell number relative to that of DAPI-positive nuclei. $^*P < 0.01$ versus nontreated cells, $^\#P < 0.05$ versus H_2O_2-treated cells without G-CSF ($n = 3$). (c) G-CSF prevents H_2O_2-induced downregulation of Bcl-2 expression ($n = 3$). (d) Inhibition of antiapoptotic effects of G-CSF by Adeno-dnStat3. Bar graphs represent quantitative analysis of the apoptotic cell number relative to the total cell number. $^*P < 0.001$ versus H_2O_2 (–)/G-CSF (–), $^\#P < 0.001$ versus H_2O_2 (+)/G-CSF (–), $^\dagger P < 0.001$ versus H_2O_2 (+)/G-CSF (+)/Adeno-LacZ ($n = 3$).

(Fig. 2a,b). To investigate the molecular mechanism of how G-CSF exerts an antiapoptotic effect on cultured cardiomyocytes, we examined expression of the Bcl-2 protein family, known target molecules of the Jak-Stat pathway[24], by western blot analysis. Expression levels of antiapoptotic proteins such as Bcl-2 and Bcl-xL were lower when cardiomyocytes were subjected to H_2O_2 (Fig. 2c and data not shown), and this reduction was considerably inhibited by G-CSF pretreatment (Fig. 2c). AG490, an inhibitor of Jak2, abolished G-CSF-induced Bcl-2 expression (Fig. 2c) but did not affect its basal levels (Supplementary Fig. 3 online), suggesting a crucial role of the Jak-Stat pathway in inducing survival of cardiomyocytes by G-CSF. To further elucidate the involvement of the Jak-Stat pathway in the protective effects of G-CSF on cardiomyocytes, we transduced cultured cardiomyocytes with adenovirus encoding dominant-negative Stat3 (Adeno-dnStat3). G-CSF treatment significantly reduced apoptosis induced by H_2O_2 in Adeno-LacZ-infected cardiomyocytes (Fig. 2d). This effect was abolished by introduction of Adeno-dnStat3 (Fig. 2d), suggesting that Stat3 mediates the protective effects of G-CSF on H_2O_2-induced cardiomyocyte apoptosis.

Effects of G-CSF on cardiac function after myocardial infarction

Consistent with the *in vitro* data, G-CSF enhanced activation of Stat3 in the infarcted heart (Fig. 3a). Notably, the levels of G-CSFR were markedly increased after myocardial infarction in cardiomyocytes (Supplementary Fig. 4 online), which may enhance the effects of G-CSF on the infarcted heart. To elucidate the role of G-CSF-induced Stat3 activation in cardiac remodeling, we produced myocardial infarction in transgenic mice which express dominant-negative Stat3 in cardiomyocytes under the control of the α-myosin heavy chain promoter (dnStat3-Tg). Administration of G-CSF was started at the time of coronary artery ligation (day 0) until day 4 in transgenic mice; we termed this group Tg-G mice. A control group of dnStat3-Tg mice given myocardial infarction received saline (Tg-cont) instead of G-CSF. We also included two groups of wild-type mice given myocardial infarction treated with G-CSF (Wt-G) or saline (Wt-cont). At 2 weeks after myocardial infarction, we assessed the morphology by histological analysis and measured cardiac function by echocardiography and catheterization analysis. The infarct area was significantly smaller in the Wt-G group than the Wt-cont group (Fig. 3b). The Wt-G group also showed less left ventricular end-diastolic dimension (LVEDD) and better fractional shortening as assessed by echocardiography, and lower end-diastolic pressure (LVEDP) and better $+dp/dt$ and $-dp/dt$ as assessed by cardiac catheterization compared with Wt-cont (Fig. 3c). The beneficial effects of G-CSF on cardiac function were dose dependent and were significantly reduced by delayed start of the treatment (Fig. 3d,e and Supplementary Fig. 5 online). Moreover, its favorable effects on cardiac function became evident within 1 week after the treatment (Fig. 3f). Disruption of the Stat3 signaling pathway in cardiomyocytes abolished the protective effects of G-CSF. There was no significant difference in LVEDD, fractional shortening, LVEDP, $+dp/dt$ and $-dp/dt$ between Tg-G and Tg-cont (Fig. 3c). We obtained similar results from infarcted female hearts (Fig. 3g). These results suggest that G-CSF protects the heart after myocardial infarction at least in part by directly activating Stat3 in cardiomyocytes, which is a gender-independent effect. We have previously shown that treatment with G-CSF significantly ($P < 0.05$) decreased myocardial infarction–related mortality of wild-type mice[2]. In contrast, there were no significant differences in mortality between G-CSF-treated and saline-treated dnStat3-Tg mice (data not shown).

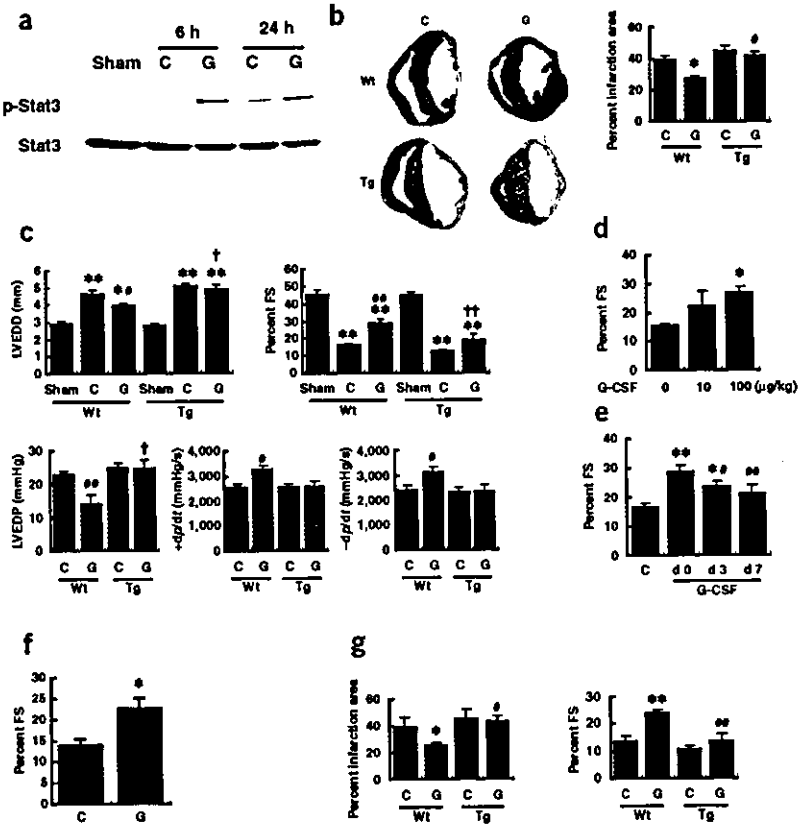

Figure 3 Effects of G-CSF on cardiac function after myocardial infarction. (**a**) Stat3 activation in the infarcted hearts. We operated on wild-type mice to induce myocardial infarction and treated them with G-CSF (G) or saline (C). (**b**) Masson trichrome staining of wild-type (Wt) and dnStat3-Tg (Tg) hearts. $^{*}P < 0.001$ versus Wt-cont, $^{\sharp}P < 0.001$ versus Wt-G ($n = 11$–15). (**c**) G-CSF treatment preserves cardiac function after myocardial infarction. $^{*}P < 0.01$, $^{**}P < 0.001$ versus sham; $^{\sharp}P < 0.05$, $^{\sharp\sharp}P < 0.001$ versus Wt-cont; $^{\dagger}P < 0.01$, $^{\dagger\dagger}P < 0.001$ versus Wt-G ($n = 10$–15 for echocardiography and $n = 5$ for catheterization analysis). (**d**) Dose-dependent effects of G-CSF. FS, fractional shortening. $^{*}P < 0.01$ versus saline-treated mice (G-CSF = 0)($n = 12$–14). (**e**) Wild-type mice were operated to induce myocardial infarction and G-CSF treatment (100 μg/kg/d) was started from the indicated day for 5 d. $^{*}P < 0.05$, $^{**}P < 0.001$ versus saline-treated mice (C); $^{\sharp}P < 0.05$, $^{\sharp\sharp}P < 0.01$ versus mice treated at day 0 (d 0) ($n = 11$–12). (**f**) Effects of G-CSF on cardiac function at 1 week. $^{*}P < 0.05$ versus control ($n = 3$). (**g**) Effects of G-CSF on cardiac function of female mice. $^{*}P < 0.05$, $^{**}P < 0.001$ versus Wt-cont; $^{\sharp}P < 0.05$, $^{\sharp\sharp}P < 0.005$ versus Wt-G ($n = 4$–5).

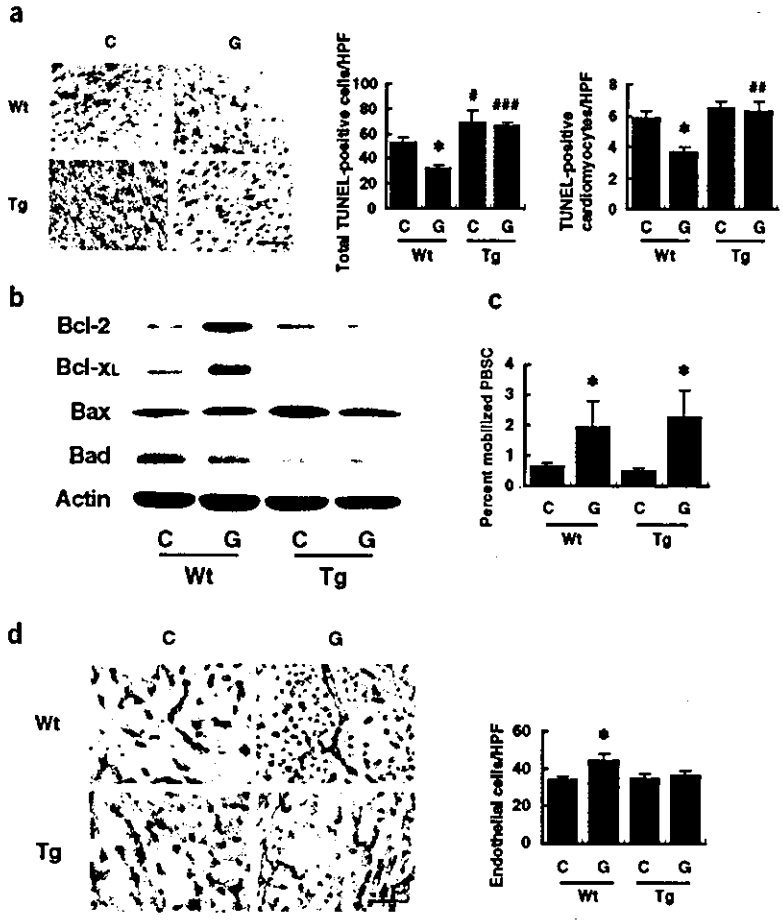

Figure 4 Mechanisms of the protective effects of G-CSF. (**a**) TUNEL staining (brown nuclei) in the infarcted hearts. The graphs show quantitative analyses for total TUNEL-positive cells (left graph) and TUNEL-positive cardiomyocytes (right graph) in infarcted hearts. $^{*}P < 0.01$ versus Wt-cont; $^{\#}P < 0.05$, $^{\#\#}P < 0.005$, $^{\#\#\#}P < 0.001$ versus wild-type mice with the same treatment ($n = 5$–7). Scale bar, 100 μm. (**b**) Infarcted hearts treated with G-CSF (G) or saline (C) were analyzed for expression of Bcl-2, Bcl-xL, Bax and Bad by western blotting ($n = 3$). (**c**) Mobilization of hematopoietic stem cells into peripheral blood (PBSC). $^{*}P < 0.05$ versus saline-treated mice ($n = 4$). (**d**) Capillary endothelial cells were identified by immunohistochemical staining with anti-PECAM antibody in the border zone of the infarcted hearts. Scale bar, 100 μm. The number of endothelial cells was counted and shown in the graph ($n = 6$–8). $^{*}P < 0.05$.

Mechanisms of the protective effects of G-CSF

Our *in vitro* results suggest that the protective effects of G-CSF on cardiac remodeling after myocardial infarction can be attributed in part to reduction of cardiomyocyte apoptosis. To determine whether the Stat3 pathway in cardiomyocytes mediates the antiapoptotic effects of G-CSF on the ischemic myocardium, we carried out TUNEL labeling of left ventricular sections 24 h after myocardial infarction in wild-type mice and dnStat3-Tg mice. Although the number of TUNEL-positive cells was significantly less in the Wt-G group than the Wt-cont group, G-CSF treatment had no effect on cardiomyocyte apoptosis in dnStat3-Tg mice (**Fig. 4a**). The effects of G-CSF on apoptosis after myocardial infarction were also attenuated when mice were treated with AG490 (**Supplementary Fig. 6** online). Myocardial infarction–related apoptosis was significantly increased in the Tg-cont group and AG490-treated wild-type mice compared with Wt-cont mice (**Fig. 4a** and **Supplementary Fig. 6** online), suggesting that endogenous activation of Stat3 has a protective role in the infarcted heart, as reported previously[25]. It is noteworthy that G-CSF treatment inhibited apoptosis of noncardiomyocytes including endothelial cells and that this inhibition was abolished in dnStat3-Tg mice (**Fig. 4a** and data not shown). To investigate the underlying molecular mechanism of the antiapoptotic effects of G-CSF *in vivo*, we examined expression of the Bcl-2 protein family by western blot analysis. Consistent with our *in vitro* results, expression of antiapoptotic proteins such as Bcl-2 and Bcl-xL was significantly increased in the Wt-G group at 24 h after myocardial infarction compared with the Wt-cont group, whereas expression of the proapoptotic proteins Bax and Bad was not affected by the treatment (**Fig. 4b**). In contrast, expression levels of antiapoptotic proteins were not increased by G-CSF in the Tg-G group (**Fig. 4b**). Immunohistochemical analysis also showed increased expression of Bcl-2 in the infarcted heart of the Wt-G group but not of the Tg-G group (**Supplementary Fig. 7** online).

To determine the effects of G-CSF on mobilization of stem cells, we counted the number of cells positive for both Sca-1 and c-kit in peripheral blood samples from mice treated with G-CSF or saline. The G-CSF treatment similarly increased the number of double-positive cells in wild-type mice and dnStat3-Tg mice (**Fig. 4c**). To examine the impact of G-CSF on cardiac homing of bone marrow cells, we transplanted bone marrow cells derived from GFP transgenic mice into wild-type and dnStat3-Tg mice, produced myocardial infarction and treated with G-CSF or saline. FACS analysis showed that G-CSF did not increase cardiac homing of bone marrow cells in wild-type and dnStat3-Tg mice (**Supplementary Fig. 8** online). We have shown that cardiac stem cells, which are able to differentiate into cardiomyocytes, exist in Sca-1-positive populations in the adult myocardium[26]. But G-CSF treatment did not affect the number of Sca-1-positive cells in the infarcted hearts of wild-type or dnStat3-Tg mice (**Supplementary Fig. 9** online). Thus, it is unlikely that G-CSF exerts its beneficial effects through expansion of cardiac stem cells. To determine the effects of G-CSF on proliferation of cardiomyocytes, we carried out immunostaining for Ki67, a marker for cell cycling, in conjunction with a labeling for troponin T. The number of Ki67-positive cardiomyocytes was increased in the infarcted hearts of wild-type mice and dnStat3-Tg mice compared with sham-operated mice (**Supplementary Fig. 10** online). But G-CSF did not alter the number of Ki67-positive cardiomyocytes in wild-type or dnStat3-Tg mice, suggesting that G-CSF does not induce proliferation of cardiomyocytes (**Supplementary Fig. 10** online). The number of Ki67-positive cardiomyocytes was less in infarcted hearts of dnStat3-Tg mice than in those of wild-type mice, suggesting that endogenous Stat3 activity is required

for myocardial regeneration after myocardial infarction and that activation of Stat3 by G-CSF is not sufficient for cardiomyocytes to enter the cell cycle in infarcted hearts of wild-type mice (**Supplementary Fig. 10** online). In contrast, G-CSF treatment significantly increased the number of endothelial cells in the border zone of the infarcted hearts (**Fig. 4d**). This increase was attenuated in dnStat3-Tg mice, indicating that the increased vascularity is mediated by Stat3 activity in cardiomyocytes and may partially account for the beneficial effects of G-CSF on the infarcted hearts. Taken together with the result that G-CSF-induced inhibition of noncardiomyocyte apoptosis was also mediated by the Stat3 signaling pathway in cardiomyocytes (**Fig. 4a**), these findings imply that communication between cardiomyocytes and noncardiomyocytes regulates each others' survival.

To further test whether G-CSF acts directly on the heart, we examined the effects of G-CSF treatment on cardiac function after ischemia-reperfusion injury in a Langendorff perfusion model. The isolated hearts underwent 30 min total ischemia followed by 120 min reperfusion with the perfusate containing G-CSF (300 ng/ml) or vehicle, and left ventricular developed pressure (LVDP, measured as the difference between systolic and diastolic pressures of the left ventricle) and LVEDP were measured. There were no significant differences in basal hemodynamic parameters including heart rate, left ventricular pressure, LVEDP and positive and negative d*p*/d*t*, between the control group and G-CSF group (**Table 1**). After reperfusion, however, G-CSF-treated hearts started to beat earlier than those of the control group (**Fig. 5a**). At 120 min after reperfusion, contractile function (LVDP) of G-CSF-treated hearts was significantly better than that of control hearts (**Fig. 5a**). Likewise, diastolic function (LVEDP) of G-CSF-treated hearts was better than that of control hearts (**Fig. 5a**). After ischemia-reperfusion, there was more viable myocardium (red lesion) in G-CSF-treated hearts than control hearts (**Fig. 5b**). The size of the infarct (white lesion) was significantly smaller in G-CSF-treated hearts than in control hearts (**Fig. 5b**).

Table 1 Basal hemodynamic parameters

	Control ($n = 7$)	G-CSF ($n = 7$)
HR (b.p.m.)	326 ± 34	334 ± 24
LVP (mmHg)	121.8 ± 24	117.3 ± 32
LVEDP (mmHg)	4.3 ± 1.3	4.5 ± 1.6
+d*p*/d*t* (mmHg/s)	7,554 ± 643	7,657 ± 377
−d*p*/d*t* (mmHg/s)	6,504 ± 638	6,670 ± 602

HR, heart rate; b.p.m., beats per minute; LVP, left ventricular pressure; LVEDP, left ventricular end-diastolic pressure; +d*p*/d*t* and −d*p*/d*t*, positive and negative first derivatives for maximal rates of left ventricular pressure development.

DISCUSSION

In the present study, G-CSFR was found to be expressed on cardiomyocytes and cardiac fibroblasts, and G-CSF activated Jak2 and the downstream signaling molecule Stat3 in cultured cardiomyocytes. Treatment with G-CSF protected cultured cardiomyocytes from apoptotic cell death possibly through upregulation of Bcl-2 and Bcl-xL expression, suggesting that G-CSF has direct protective effects on cardiomyocytes through G-CSFR and the Jak-Stat pathway. This idea is further supported by the *in vivo* experiments. G-CSF enhanced Stat3 activity and increased expression of Bcl-2 and Bcl-xL in the infarcted heart where G-CSFR was markedly upregulated, thereby preventing cardiomyocyte apoptosis and cardiac dysfunction. These effects of G-CSF were abolished when Stat3 activation was disrupted in cardiomyocytes, suggesting that a direct action of G-CSF on cardiomyocytes has a crucial role in preventing left ventricular remodeling after myocardial infarction. Because noncardiomyocytes also expressed G-CSFR, the possibility exists that activation of G-CSF receptors on these cells modulates the beneficial effects of G-CSF on infarcted hearts.

The mobilization of bone marrow stem cells (BMSC) to the myocardium has been considered to be the main mechanism by which G-CSF ameliorates cardiac remodeling after myocardial infarction[1,6–8]. In this study, we showed that G-CSF reduces apoptotic cell death and effectively protects the infarcted heart, which is dependent on its direct action on cardiomyocytes through the Stat3 pathway. This antiapoptotic mechanism seems to be more important than induction of BMSC mobilization, because disruption of

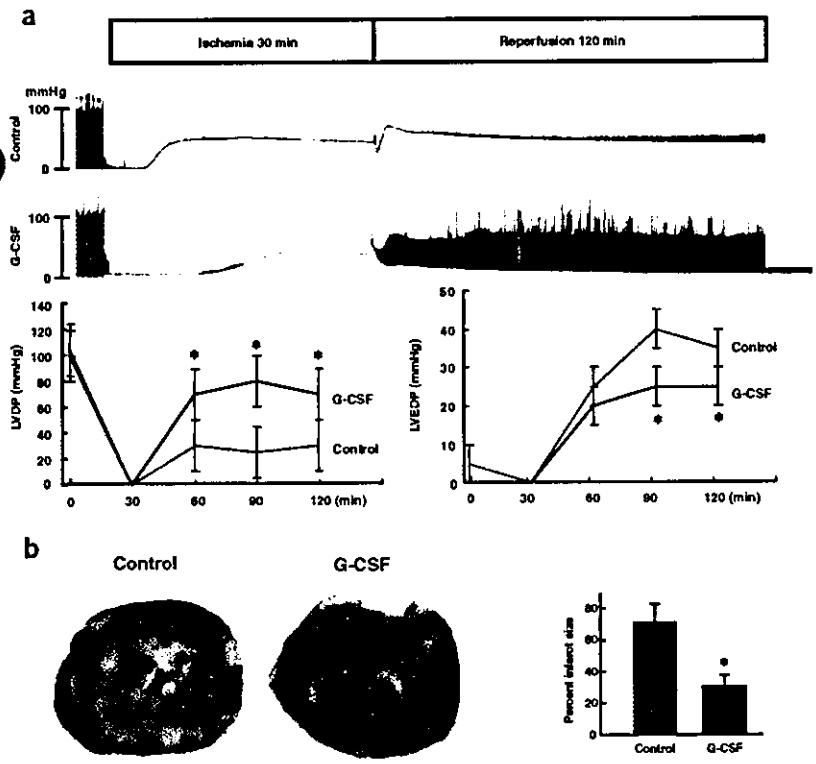

Figure 5 Direct effects of G-CSF on cardiac function after ischemia-reperfusion injury. (a) Representative left ventricular pressure records of control and G-CSF-treated hearts are shown (upper panel). The graphs show changes in LVDP (left) and LVEDP (right) during ischemia-reperfusion. *$P < 0.05$ versus control hearts ($n = 7$). (b) The photographs show representative TTC staining of control hearts (Control) and G-CSF-treated hearts (G-CSF) after ischemia-reperfusion. The graph indicates myocardial infarct sizes for control hearts (Control) and G-CSF-treated hearts (G-CSF). Infarct sizes were calculated as described in **Supplementary Methods** online. *$P < 0.05$ versus control hearts ($n = 7$).